Editors' Suggestion

Dynamic mode structure of active turbulence

Richard J. Henshaw [1], Olivia G. Martin [1,2] and Jeffrey S. Guasto [1,*]

[1] *Department of Mechanical Engineering, Tufts University, Medford, Massachusetts 02155, USA*

[2] *Department of Mechanical Engineering, Stanford University, Stanford, California 94305, USA*

(Received 1 September 2022; accepted 24 January 2023; published 17 February 2023)

Dense suspensions of swimming bacteria exhibit chaotic flow patterns that promote the mixing and transport of resources and signaling chemicals within cell colonies. While the importance of active turbulence is widely recognized, the structure and dynamics of the resulting collective flows are the subject of intense investigation. Here, we combine microfluidic experiments with proper orthogonal decomposition (POD) analysis to quantify the dynamical flow structure of this model active matter system under a variety of conditions. In isotropic quasi-two-dimensional turbulence, the modal analysis encompasses the most energetic spatiotemporal flow structures across a range of suspension activity levels and benchmarks the potential for low-dimensional order representations of active turbulence. In confined geometries, POD analysis illustrates the role of boundary interactions for the transition to bacterial turbulence, and it quantifies the evolution of coherent active structures in externally applied flows. Beyond establishing the physical flow structures underpinning the complex dynamics of bacterial turbulence, the low-dimensional representation afforded by this modal analysis will facilitate data-driven modeling of active turbulence.

DOI: 10.1103/PhysRevFluids.8.023101

I. INTRODUCTION

The collective motion of concentrated suspensions of swimming bacteria and self-propelled actin filaments are typical of a broad class of active systems, ranging from flocking birds and schooling fish down to micron-sized synthetic active colloids [1–5]. Such active suspensions regulate fundamental ecological and biological processes, for example, in the gut microbiome of the human gastrointestinal tract [6], as well as the mitotic spindle structure during cell division [7]. At high concentrations, swimming bacteria form emergent jetlike flow structures and eddies [8–12], which are correlated over length scales that are 1 order of magnitude larger than the individual cells and enhance the colony mobility [13]. These chaotic flow patterns—termed as active turbulence [14]—are reminiscent of classical, inertial turbulence [15] and exhibit a range of novel physical properties, such as enhanced material transport [13,16], boundary-induced pattern formation [17,18], and reduced viscosity and superfluidlike behavior [19,20]. Collective flows are highly dependent on the physical properties of their constituent agents, where variations in cell size, swimming speed, suspension density, nutrient availability, media or substrate, and viscosity can alter the nature of the cell motion [11,21–24]. Apart from traditional, bulk statistical measures and velocity spectra [3,4,11,12], relatively little experimental progress has been made in understanding the underlying flow structure of active turbulence, especially in the presence of boundaries and ambient flows. A host of theoretical and computational models have been proposed to explain these phenomena [4,25–28], as well as the onset of active turbulence under confinement [29], and recent

*To whom correspondence should be addressed: Jeffrey.Guasto@tufts.edu

work using machine-learning approaches to uncover the equations of motion for active turbulence are promising [30]. However, the vast experimental parameter space and necessity for big data sets to characterize these chaotic systems complicate data-driven discovery through simulations. Thus, establishing new approaches to characterize the dynamic structure of active turbulence and provide compact reduced-order representations are essential, for example, to understand the movement ecology of collective microbial motion [31] and to design and engineer new classes of active materials [32].

Inspired by approaches from inertial turbulence, we apply proper orthogonal decomposition (POD) to analyze the spatiotemporal dynamics of self-generated bacterial turbulence flows. POD—also known as PCA or the Karhunen-Loève procedure [33–35]—computes an orthogonal basis set that optimally represents the fluid velocity field, an approach that has been instrumental, for example, in the development of reduced-order flow models [34,36,37]. In POD, a velocity field $\mathbf{u}(\mathbf{x}, t)$ at N discrete times is represented by a linear combination of N orthonormal spatial modes, $\phi_n(\mathbf{x})$, as

$$\mathbf{u}(\mathbf{x}, t) = \sum_{n=1}^{N} A_n(t)\phi_n(\mathbf{x}), \tag{1}$$

where $A_n(t) = a_n(t)\sqrt{\lambda_n}$, $a_n(t)$ is a normalized temporal coefficient and λ_n is the spatiotemporal average kinetic energy for a given mode [37]. This process is achieved through singular value decomposition (see Appendix A 2) [38], which ranks the spatial modes, $\phi_n(\mathbf{x})$, by decreasing energy, λ_n. Despite the striking similarities between inertial and active turbulence, POD techniques have seen limited applications in soft matter and low Reynolds number flows [39–42].

In this work, we use microfluidic experiments to measure the chaotic self-generated flow fields of bacterial turbulence under a variety of conditions, which we then decompose using modal analysis to quantify their flow structure and dynamics. Bacterial turbulence is first investigated far from lateral boundaries (quasi-two-dimensional), where we determine the effects of varying cell activity [4,12] on the spatiotemporal mode structure and benchmark the efficacy of data compression for active turbulence. Subsequently, we use POD to elucidate the role of boundary interactions in the transition to bacterial turbulence in confined geometries [18,29] and to quantify the evolution of coherent active structures in externally applied flows [43]. Not only does POD analysis unveil the constituent flow structures underpinning the chaotic bacterial motion in each of these physical systems, but this framework also provides an accurate and efficient representation of active turbulence with remarkably few spatial modes.

II. RESULTS AND DISCUSSION

A. Modal analysis of quasi-two-dimensional bacterial turbulence

In unbounded domains, concentrated suspensions of motile bacteria exhibit complex spatiotemporal flow patterns. Dense suspensions of motile *Bacillus subtilis* bacteria were loaded into microfluidic chambers (26 μm deep) with widely separated side walls (2 mm). The active suspensions were imaged in the center of the channel, far from the boundaries, using video microscopy for ≈1 min ($N = 6300$ frames). Time-dependent velocity fields, $\mathbf{u}(\mathbf{x}, t)$, characterizing the bacterial motion [Fig. 1(a)] were measured using particle image velocimetry (PIV; see Appendices A 1 and A 3) [18]. The resulting chaotic flows exhibit vortex structures (≈40 μm) and mean flow speeds ($\langle|\mathbf{u}|\rangle \approx 50$ μm s^{-1}) that are significantly larger than the respective length (4 μm) and swimming speed of individual cells (≈15 μm s^{-1}), consistent with previous observations [11,12].

Energy-ranked velocity field modes from POD analysis reveal the hierarchy of flow structures underlying bacterial turbulence, whereby the highest-energy modes are generally associated with the largest structures. The dominant flow structures are contained within the first several modes [Fig. 1(b), $n = 1$ and 10], followed by a transition to smaller structures [Fig. 1(b), $n = 170$] and finally higher-order modes, which capture minor perturbations to the flow field [Fig. 1(b),

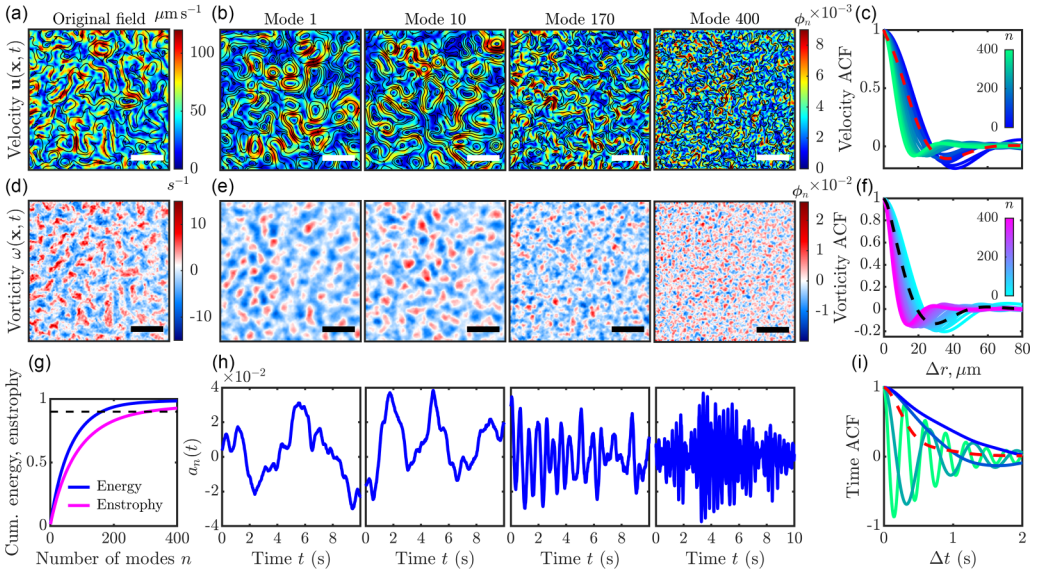

FIG. 1. POD reveals dominant spatiotemporal structures of bacterial turbulence. (a) Instantaneous measured velocity fields, $\mathbf{u}(\mathbf{x}, t)$, obtained from the collective motion of a dense suspension of swimming bacteria. (b) Sample velocity field POD modes, $\phi_n(\mathbf{x})$, organized by decreasing kinetic energy. (c) Spatial autocorrelation function (ACF) of the first 400 POD velocity field modes compared to the original flow field (dashed red), showing a decrease in the characteristic length scale as the mode number increases. (d) Instantaneous vorticity field, $\omega = \nabla \times \mathbf{u}$, corresponding to panel (a). (e) Sample vorticity field POD modes organized by decreasing enstrophy. (f) ACF of POD vorticity field modes compared to the original vorticity field (dashed black line). (g) Normalized cumulative mode energy (blue line) and enstrophy (magenta line), $C(n) = \sum_{j=1}^{n} \lambda_j / \sum_{j=1}^{N} \lambda_j$, for the first n modes. One hundred sixty-two and 305 modes are required to capture 90% (black dashed line) of the cumulative energy and enstrophy, respectively. (h) Temporal amplitudes, $a_n(t)$, of the velocity field modes in panel (b). (i) Time ACF for the mode amplitudes shown in panel (h) compared to the velocity field time ACF (dashed red line). Colors correspond to those in panel (c). Scale bars are 100 μm.

$n = 400$] as well as measurement noise. The modes appear similar across different realizations of the experiment [Appendix B, Figs. 6(a) and 6(b)], but the precise mode structure varies due to the random nature of bacterial turbulence. The autocorrelation function (ACF; Appendix A 3) of the spatial modes [Fig. 1(c)] illustrates an ordering generally from large to small flow structures with decreasing mode energy (increasing n). Furthermore, the highest-energy modes encompass the dominant spatial scales of the original velocity field [Fig. 1(c), dashed red].

Analogous to the velocity field, a POD analysis of the vorticity field [Fig. 1(d)], $\omega = \nabla \times \mathbf{u}$, provides an enstrophy-ranked set of vorticity modes [Fig. 1(e)]. The vorticity mode ACFs clearly illustrate a similar refinement of the modal vortex size [Fig. 1(f)] with decreasing enstrophy. Considering their cumulative information content [Fig. 1(g)], from the full set of 6300 modes only $N_{\mathrm{KL}} = 162$ modes (2.5%) and 305 modes (4.8%) for the energy and enstrophy, respectively, are required to form the Karhunen-Loève (KL) dimension [44], which captures 90% of the total information content. The larger number of modes for the latter suggests that enstrophy is more equally distributed across flow structures compared to the kinetic energy, although this effect may be exacerbated by numerical gradients used to calculate the enstrophy. Importantly, the dynamics of bacterial turbulence in this isotropic, quasi-two-dimensional (quasi-2D) system are accurately captured via a modal representation comprising less than 5% of the size of the original flow field data set. This extremely efficient data compression compares very well to existing high-Reynolds number systems, where 10–60% of the modes are typically used for flow field reconstruction with cumulative energy lower than that demonstrated here [45–49].

Beyond the spatial structure, modal analysis provides insight into the temporal dynamics of the chaotic flow fields. The temporal coefficients, $a_n(t)$, describe the instantaneous amplitude [Fig. 1(h)] for each spatial mode [Fig. 1(b)] and fluctuate strongly in time. The ACFs of the temporal coefficients [Fig. 1(i)] show that the large, high-energy flow structures associated with low mode numbers are strongly correlated. While lower-energy modes exhibit faster initial decay rates, the envelope of their rapidly fluctuating ACF is comparable to correlation strengths of the high-energy modes and the original velocity field [Fig. 1(i), red dashed line]. Thus, POD not only provides a rigorous framework for concise low-order representations of this model active matter system, it also establishes tools to gain deeper insight into their complex structure and dynamics under a variety of physical conditions.

B. Effect of bacterial activity on mode structure and energy distribution

In addition to cell size, concentration, and other variables [11,21–24], suspension activity is a critical factor in determining the dynamics of active turbulence [50]. Bacterial activity is quantified by the mean flow speed of the suspension, $\langle|\mathbf{u}|\rangle$, and varied here in a controlled manner by exploiting the aerobic properties of the bacteria [11]. Microfluidic chambers were loaded with cells as described previously, and the bacterial suspensions were imaged periodically over ≈30 min. As oxygen was slowly depleted, the cell activity decreased from >50 μm s^{-1} to approximately the single-cell swimming speed. After this point, the cell activity decays rapidly to zero and vortices cease to form, and hence these extremely slow fields are not shown. For all activities, the kinetic energy spectra, $E(k)$, as a function of the wave number k collapse [Fig. 2(a)] to previously reported power-law behaviors [4], illustrating the robustness of these results.

Beyond classical measures of collective motion, modal analysis reveals rich changes in the structure and complexity of bacterial turbulence with cell activity, including a diminishing number of dominant modes as the cell swimming speed decreases. The characteristic length scale of the turbulent velocity fluctuations remains approximately constant across all activities (velocity correlation length range of $\delta \approx 15.4$–18.5 μm) [11,12], as shown by the spatial velocity ACF [Fig. 2(b)]. Consequently, the slowdown results in a broadening of the temporal ACF [Fig. 2(c); see also Appendix B, Fig. 5]. As the cell activity decreases, the mode structures have a qualitatively similar appearance (see Appendix B, Fig. 6). However, the energy distribution shifts to lower-order modes [Fig. 2(d)]. For example, the lowest activity examined ($\langle|\mathbf{u}|\rangle = 14.9$ μm s^{-1}) required 65% fewer modes to capture 90% of the kinetic energy relative to the most active suspensions [Fig. 2(d), inset]. This feature appears consistent with kinetic models [28], which predict that the longest wavelengths are the most unstable and have a growth rate that scales linearly with activity. Moreover, analysis of the mode correlation lengths, δ, reveals that dominant spatial modes emerge [Fig. 2(e)], which are characterized by both high energy and long correlation lengths and reflect δ for the original flow field [Fig. 2(b)].

While δ exhibits relatively minor variations across different activities, the correlation times of the mode amplitudes, τ, increase strongly with decreasing cell activity [Fig. 2(f)]. This analysis shows that the most energetic velocity field modes are also responsible for the increase in τ. POD analysis enriches observations afforded by traditional metrics [Figs. 2(a)–(c)] by identifying the associated flow structures responsible for the observed behaviors and extracts the individual mode dynamics [Figs. 2(d)–(f)]. Ultimately, insights from the POD analysis are limited due to the isotropic and random nature of bacterial turbulence in this case. However, as we illustrate below, this isotropic, latterly unbounded system benchmarks the upper bound for the spatial mode complexity, which is dramatically altered by confinement.

C. Edge modes illustrate the role of confinement in the transition to active turbulence

Boundaries play a fundamental role in regulating active turbulence [50], whereby confinement has been shown to select for vortical flow structures [17] and lead to the formation of self-organized

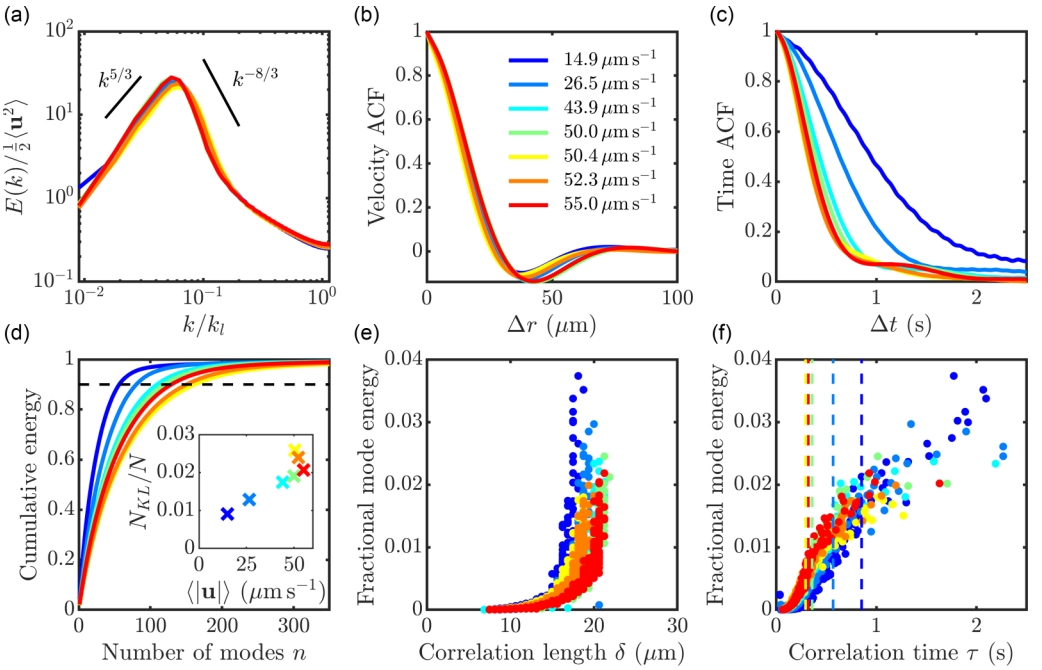

FIG. 2. Variation in bacterial turbulence structure with swimming activity. (a) Normalized kinetic energy spectra as a function of normalized wave number exhibit self-similarity and consistent power-law behavior [4] across a wide range of bacterial activity levels, $\langle |\mathbf{u}| \rangle$. The characteristic wave number is $k_l = 2\pi/l$, where $l = 4$ μm is the typical cell length. (b) Spatial velocity ACF remains constant across various cell activities. (c) Temporal velocity ACF broadens significantly as bacterial swimming activity decreases. (d) Cumulative kinetic energy contained within POD modes illustrates the relative increase in energy for low-order modes with decreasing cell activity. Black dashed line corresponds to the 90% energy KL dimension. See also Appendix B, Fig. 6. (e) Fractional mode energy $\lambda_n/\Sigma\lambda_n$ as a function of the correlation length δ of individual POD modes [$n \leqslant 400$; $1/e$ decay of velocity ACF; Fig. 1(c)] shows that, generally, the most energetic modes typically correspond to the largest spatial scales, which remain constant across bacterial activities. (f) Fractional mode energy $\lambda_n/\Sigma\lambda_n$ as a function of the correlation time τ of individual POD mode amplitudes [$n \leqslant 400$; $1/e$ decay of time ACF; Fig. 1(i)]. The most energetic modes have the largest τ values, which increase with decreasing activity. Vertical dashed lines indicate τ for time ACFs from panel (c).

flow patterns [51]. Similar to inertial turbulence, bacterial suspensions [18,52,53] and active nematics [29,52,54,55] confined in a channel exhibit a striking transition from stable flow to chaotic dynamics as the separation between lateral boundaries increases. By replicating recent experimental results [Figs. 3(a)–3(h)] [18], we extend our POD analysis to quantify the effects of confinement on bacterial turbulence. Briefly, a dense suspension of *B. subtilis* was confined laterally in a series of microfluidic "racetrack" channels (Appendix A 4) with varying width, W [Fig. 3(a)]. Strong confinements—where W is approximately less than the quasi-2D vortex size (Fig. 1)—rectify cell activity into a unidirectional flow [Fig. 3(c)], as shown by the streamwise averaged flow profile [$F(y)$; Fig. 3(f)] and normalized net flow rate [ψ; Fig. 3(b); Appendix A 4]. As W increases, vortex structures emerge [Fig. 3(d)] before giving way to chaotic dynamics [Fig. 3(e)], when W is significantly larger than the quasi-2D vortex size. The formation of vortices and the subsequent chaotic flow are typified by sinusoidal velocity profiles [Figs. 3(g)–3(h)] with strong wall velocities and a rapid decrease in ψ [Fig. 3(b)], both of which are in very good qualitative agreement with previous work [18]. Reduced-order POD representations accurately and compactly capture the emergent active velocity field behaviors across varying channel widths [Figs. 3(f)–(h)] throughout this flow transition.

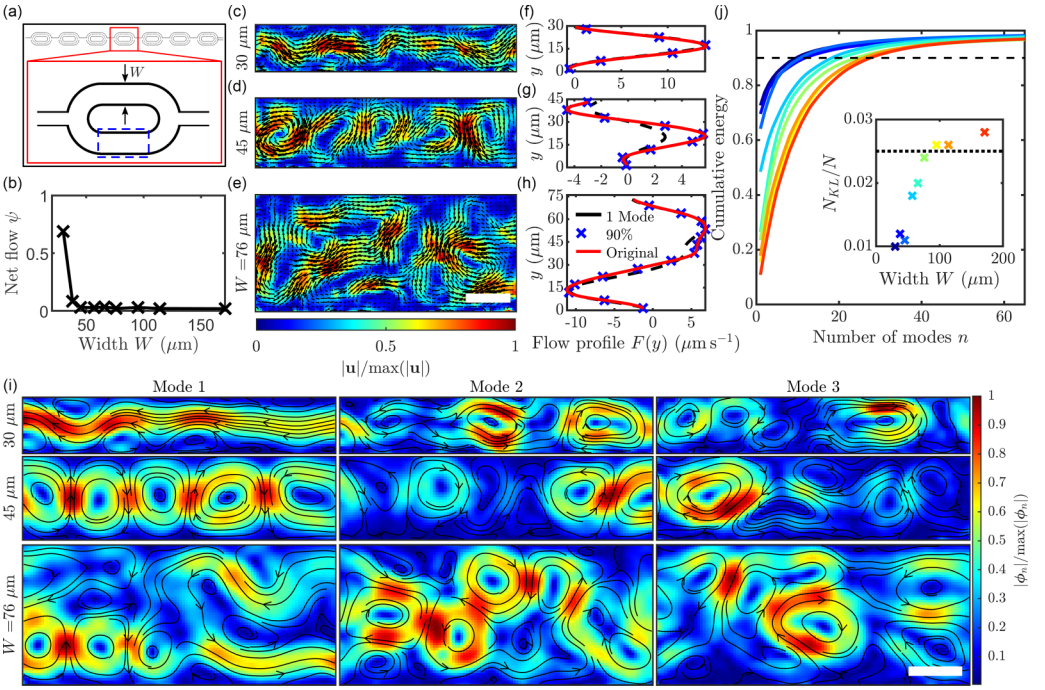

FIG. 3. POD unveils the role of edge modes in the transition to active turbulence under confinement. (a) Schematic of microfluidic racetrack channels of varying widths (30 μm $\leqslant W \leqslant$ 171 μm) to study effects of confinement on bacterial turbulence [18]. Straight observation regions (dashed blue line) were fixed at 150 μm long. (b) Normalized net flow rate ψ illustrates the transition from unidirectional flow for small W to turbulent flow at large W, which agrees well with previous studies [18]. (c)–(e) Normalized instantaneous velocity fields for various channel widths. Scale bar, 25 μm. (f)–(h) Streamwise averaged flow profiles, $F(y)$, for original flow fields [red line; corresponding to panels (c)–(e)] compared to a 90% POD reconstruction (blue crosses) and single mode reconstruction (black dashed line) using modes from panel (i). (i) The three highest-energy (normalized) POD modes for various W. Scale bar, 25 μm. (j) Cumulative POD mode energy increases with decreasing channel width. Black dashed line indicates the 90% energy KL dimension. (Inset) N_{KL} as a fraction of the total number of modes, N, plateaus as the channel approaches quasi-2D conditions (black dotted line).

The topologies of the spatial modes, $\phi_n(\mathbf{x})$, reveal the fundamental flow structures underpinning the effects of confinement on suspension dynamics [Fig. 3(i)]. For the strongest confinement examined, the highest-energy mode encapsulates the nearly steady, stable flow [Fig. 3(i), $W = 30$ μm], representing >70% of the total kinetic energy [Fig. 3(j)]. At intermediate channel widths, mode 1 highlights the emergent vortex chain, where higher-order modes have similar topologies that describe streamwise fluctuations of the vortices [Fig. 3(i), $W = 45$ μm]. Importantly, in weak confinement prior to transitioning to isotropic, quasi-2D turbulence, the most energetic mode reveals coherent, near-wall activity [mode 1; Fig. 3(i), $W = 76$ μm, see also Appendix B, Fig. 7]. Such edge modes are consistent with both previous experimental observations of confined bacterial suspensions [18] and the pinning and stabilization of defects to walls in active nematics simulations [50], which are thought to regulate the transition to active turbulence. In contrast, lower-energy modes (modes 2–3) describe chaotic fluctuations in the center of the channel away from boundaries, akin to quasi-2D turbulence modes [Fig. 1(b)]. These highly energetic modes [Fig. 3(i)] also bear striking resemblance to the unstable eigenmodes predicted by kinetic models [56], suggesting that POD and related techniques [57] may provide direct insights into the stability of experimentally measured active suspensions. The kinetic energy distribution across modes is a strong indicator of the onset of bacterial turbulence under confinement [Fig. 3(j)], which is exemplified by the rapid

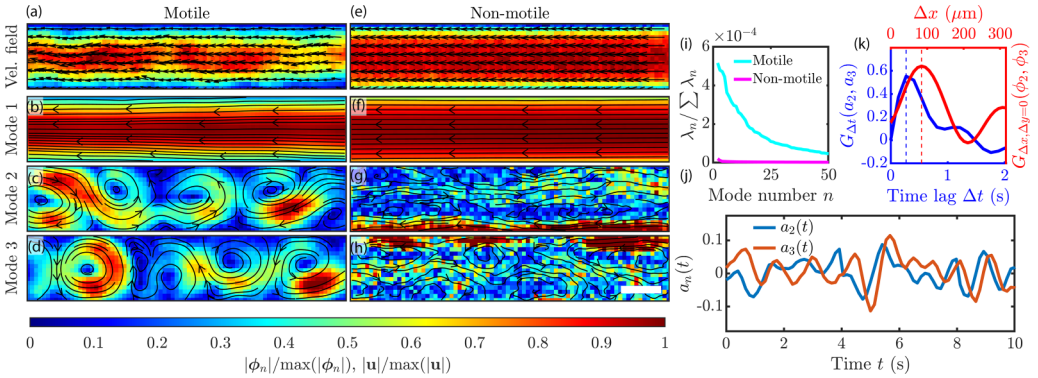

FIG. 4. POD modes capture intermittent bacterial turbulence in externally applied flows. (a) Instantaneous normalized velocity field of a dense, active bacterial suspension flowed through a rectangular microchannel exhibits strong flow intermittency. Velocity field data obtained from previously published work [43]. (b)–(d) Three most energetic (normalized) POD modes for the motile suspension in panel (a). Mode 1 resembles a Poiseuille-like background flow, whereas modes 2 and 3 are antiphase vortices that capture traveling active flow structures. (e) Instantaneous normalized velocity field of a nonmotile cell suspension under the same conditions as in panel (a), which shows a near-parabolic flow profile. (f)–(h) Three most energetic (normalized) POD modes for the nonmotile suspension in panel (e). Mode 1 resembles a Poiseuille-like background flow, while modes 2 and 3 capture only minor noise fluctuations. Scale bar, 100 μm. (i) Fractional POD mode energy for the motile (cyan) and nonmotile (magenta) suspensions corresponding to panels (a)–(d) and panels (e)–(h), respectively. (j) Temporal amplitudes a_2 (blue line) and a_3 (orange line) of the motile suspension, corresponding to spatial modes 2 and 3 in panels (c) and (d), respectively. (k) Phase shifts of the temporal mode amplitudes (blue) and spatial modes (red) for modes 2 and 3 of the motile suspension are indicative of the traveling turbulent structures shown in panel (a). $G_{\Delta t}$ is the temporal cross-correlation of mode amplitudes shown in panel (j), and $G_{\Delta x,\Delta y=0}$ is the spatial cross-correlation in the streamwise direction of POD modes shown in panels (c) and (d).

drop of the kinetic energy in mode 1 from 70% to 10% as W increases from 30 to 171 μm. Moreover, the number of modes N_{KL} to capture 90% of the system energy exhibits a striking increase with W [Fig. 3(j), inset] that plateaus at $W = 95$ μm (or ≈2.5 vortex lengths in the quasi-2D). The fractional N_{KL} for large W is consistent with the benchmark established in the previous quasi-2D turbulence results [i.e., 2.5% of the total modes; Fig. 3(j), inset, dashed line; see also Fig. 1] and indicates that the system has reached the fully chaotic regime.

D. Evolution of active turbulence structures in externally driven flow

Driven ambient flows are known to strongly modify the dynamics of active suspensions [43,58,59], leading to novel rheological [19,20] and transport [43] properties. Pressure-driven flows of dense, swimming bacterial suspensions through microfluidic channels were recently observed to exhibit significant flow intermittency [43]. Active vortex structures interact with the imposed external flow to produce sporadic periods of near-parabolic and pluglike flow in motile suspensions of *B. subtilis* [Fig. 4(a)], compared to nonmotile cells with steady flow [Fig. 4(e)]. Here, we investigate this phenomenon through a POD analysis of previously published data [43]. The most energetic velocity field mode for the motile [Fig. 4(b)] and nonmotile [Fig. 4(f)] suspensions are both representative of the parabolic background flow. For the active suspension, vortex chain structures [Figs. 4(c) and 4(d)] characterize higher-order modes ($n \geqslant 2$) responsible for the observed flow intermittency. In contrast, the featureless higher-order modes for the nonmotile cells [Figs. 4(g) and 4(h)] make up a comparatively minute fraction of the total kinetic energy [Fig. 4(i)], commensurate with their steady, homogeneous flow. The nontrivial higher-order modes of the swimming bacterial

suspension also give direct insights into the dynamics of the active flow structures. The vortex chain modes $\phi_2(\mathbf{x})$ and $\phi_3(\mathbf{x})$ both appear periodic in space with a wavelength of $\ell = 320$ μm, and a cross-correlation analysis reveals a phase difference of $\Delta x = 84.5$ μm [Fig. 4(k)]. Similarly, the temporal coefficients [Figs. 4(j) and 4(k)] $a_2(t)$ and $a_3(t)$ exhibit a period and phase difference $T = 1.27$ s and $\Delta t = 0.333$ s, respectively. Similar to Fourier mode analysis, a linear combination of (minimum) two orthogonal POD modes [Figs. 4(c) and 4(d)] can be used to describe the propagation of turbulent flow structures. Hence, we estimate the propagation velocity of the observed intermittent flow features [Fig. 4(a)] as a phase velocity of $v_P = \ell/T \approx 252$ μm s^{-1}. This result is comparable to the flow structure velocity (≈235 μm s^{-1}) measured by manual tracking (see Appendix A 5) [43]. A principle application of POD is the identification of coherent flow structures [60–63], which is effectively demonstrated here in the case of active turbulence.

III. CONCLUSION

In this work, we established the application of proper orthogonal decomposition to gain physical insights into the collective motion of dense suspensions of swimming bacteria. Far from boundaries, POD analysis of quasi-2D bacterial turbulence revealed that the spatial and temporal structure of the underlying velocity field modes strongly correlated with kinetic energy, which naturally ranks the mode structures in decreasing size. Decreasing cell activity shifts energy to lower-order modes that are responsible for increasing the correlation time [4,12]. For confined cell suspensions, our results accurately capture the transition to chaotic flow [18], and the resulting velocity field modes illustrate the importance of boundary interactions in regulating the dynamics, as predicted by active nematics simulations [29]. In external flows, higher-order velocity field modes describe the propagation of coherent active flow structures that are responsible for the observed flow intermittency [43]. Despite their prevalence in inertial turbulence and macroscale flow applications [37], the potential insights gained from POD and related techniques in microscopic flows have largely been overlooked, due to the typically linear behavior of low-Reynolds number flows. However, as illustrated here, the nonlinear, chaotic nature of active matter flows presents copious opportunities for mode analysis techniques to yield insights into the dynamics and potentially the stability [57] of these complex systems. For example, beyond the effects of cell activity, POD analysis could provide additional insights into the effects of cell size, suspension density, nutrient availability, media or substrate, and viscosity on the structure [11,21–24] and movement ecology [31] of collective motion. Furthermore, the compact descriptions of flow field data afforded by POD have recently been used in applications for machine learning of hydrodynamic equations [30], classification of wakes [64], and identification of ice flow drivers in glaciological processes [65]. As demonstrated by our present work, POD also provided an efficient, highly-compact description of experimental data for collective bacterial motility, where we anticipate that such low-dimensional representations will help facilitate future data-driven models of active turbulence [66,67].

ACKNOWLEDGMENTS

We thank E. Secchi for generously providing the data used in Fig. 4, and we thank M. R. Stehnach for assistance with the microfluidic device fabrication for Fig. 3. We also thank H. Wioland, J. Dunkel, M. C. Roffin, S. Yamanidouzisorkhabi, and I. Bischofberger for valuable discussions, and we thank L. Thorens for comments on the manuscript. This work was supported by NSF Grants No. CAREER CBET-1554905 and No. OCE-1829827.

R.J.H., O.G.M., and J.S.G. designed the research; R.J.H. conducted the experiments; R.J.H. and O.G.M. analyzed the data; and R.J.H., O.G.M., and J.S.G. wrote the paper.

The authors declare no conflicting interests.

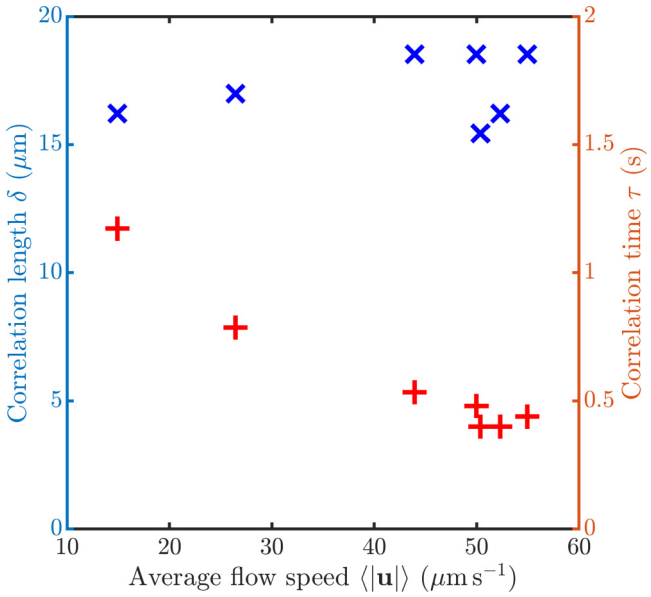

FIG. 5. Variations in the velocity correlation length and time scales with cell activity. As the suspension activity (proxied by average flow speed $\langle|\mathbf{u}|\rangle$) decreases, the correlation length δ (blue crosses) remains approximately constant, which is consistent with previous reports [11], but the correlation time τ (red pluses) increases.

APPENDIX A: METHODS

1. Cell culturing

Wild-type *Bacillus subtilis* bacteria (strain OI1084) were taken from −80 °C frozen stock and streaked onto 1.5% agar plates prepared with Terrific Broth (TB, Sigma). Plates were incubated at 25 °C for 24 h, after which time a single colony from the plate was used to inoculate an overnight liquid TB culture at 30 °C with shaking (200 rpm). The bacterial suspension was then subcultured (1.5 ml of cell culture into 60 ml of prewarmed TB) and grown at 35 °C and 200 rpm for 6 h to mid-log phase ($OD_{600} \approx 0.2$). Immediately prior to experiments, dense cell suspensions ($\sim 10^{10}$ cells ml^{-1}) were prepared by centrifugation at 5000 g for 5 min, and the pellet was resuspended with 2 µl of fresh TB media.

2. Microfluidics and image analysis

Polydimethlysiloxane (PDMS) microfluidic channels were fabricated through soft lithography [68] and plasma bonded to No. 1 thickness glass coverslips. The PDMS channels were thinly cast to ensure ample diffusion of oxygen to the bacterial suspension and prolonged cell activity. Dense cell suspensions were gently loaded into the microfluidic devices via pipette, and the channel inlet and outlet were sealed with wax to prevent residual flows. For all experiments, bacterial suspensions were imaged with brightfield illumination on an inverted microscope (Nikon Ti-E) using an sCMOS camera (Zyla 5.5, Andor Technology). Time-resolved velocity fields, $\mathbf{u}(\mathbf{x}, t)$, of the bacterial suspensions were measured by performing particle image velocimetry (PIV) using PIVLAB [69] implemented in MATLAB. The subsequent velocity fields were then lightly smoothed using a Guassian kernel with a standard deviation of one PIV pixel (1.73 µm) in space and one frame (9.5 ms) in time. Vorticity fields, $\omega(\mathbf{x}, t)$, were computed from measured velocity fields using central differencing (MATLAB). The POD was performed on the resulting velocity and vorticity fields using built-in singular value decomposition functions in MATLAB.

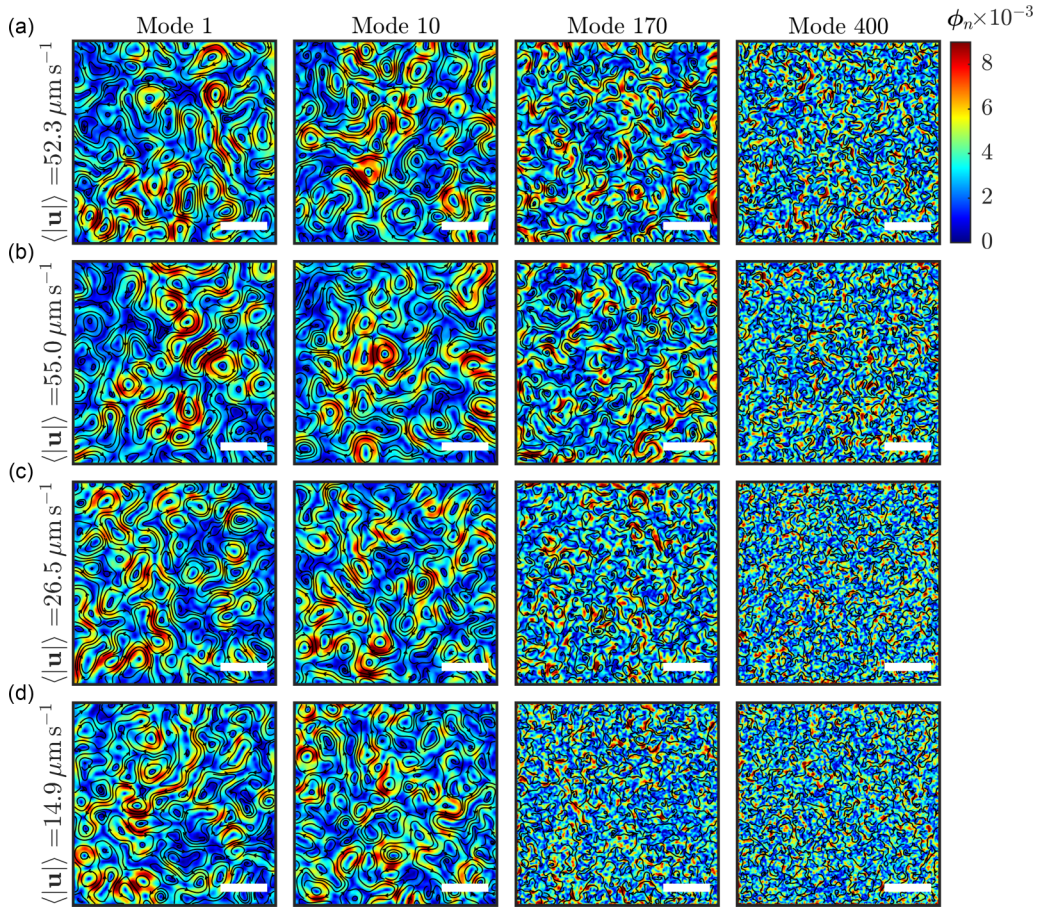

FIG. 6. Demonstration of mode structure changes with decreasing activity [rows (a)–(d)] and increasing mode numbers (columns; see also Fig. 2). (a, b) Two different experimental realizations with similar cell activity levels and similar correlation lengths and times exhibit variations in mode structure for the same mode number due to the random nature of bacterial turbulence. As the mode number increases, the typical feature size decreases towards noise (i.e., Mode 400, see also Figs. 1(b) and 1(c)]. (c, d) As the activity decreases, the dominant spatial scales are captured in a lower range of mode numbers [see also Fig. 2(e)], with noisy modes also occurring at lower mode numbers in the decomposition [see also Fig. 1(g)]. Scale bars are 100 μm.

3. Quasi-2D cell suspensions with varying activity

To capture the dynamics of dense quasi-2D bacterial suspensions in the absence of lateral wall effects (Figs. 1 and 2), large microfluidic chambers (2 mm × 2 mm × 26 μm) were prepared, where the side length corresponds to ≈80 correlation lengths of the turbulent bacterial suspension. Imaging was performed with a 20× objective (0.45 NA) at 105.5 fps. We imaged a 442-μm-square region in the center of the 2-mm-square channel, corresponding to ∼30 correlation lengths from all boundaries. Bacterial activity (Fig. 2) was varied using a previously established approach [11,12]. Briefly, the cell suspensions were imaged periodically over the course of 30 min, during which time the cell swimming speed naturally decayed due to oxygen depletion, where the decay rate of cell activity was controlled via the thickness of the PDMS device. Without the need to manipulate the cell suspension, this approach ensured that the bacterial concentration was constant across varying activity levels. Seven data sets were captured in total, which consisted of 6300 frames each (≈1 min per video) and a 2- to 3-min delay between acquisitions.

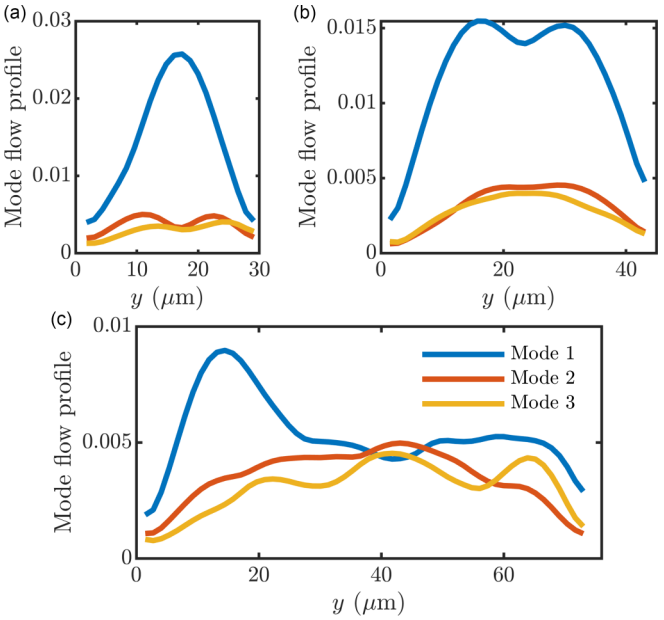

FIG. 7. Effect of confinement on individual mode flow profiles for (a) $W = 30$ μm, (b) $W = 45$ μm, and (c) $W = 76$ μm [see Fig. 3(i)]. Here, the mode flow profiles are calculated by averaging individual spatial modes along the channel, which are scaled by their respective energies [i.e., $\langle\sqrt{\lambda_n}\phi_n(x, y) \cdot \hat{\mathbf{e}}_x\rangle_{(x)}$], demonstrating the energy distribution across the y direction of the channel. At the narrowest width [panel (a); $W = 30$ μm], mode 1 contains the majority of the energy of the system [see also Fig. 3(j)] and reflects the pumping state of the system under this confinement, with the subsequent modes providing small corrections to the flow profile. In the intermediate case [panel (b); $W = 45$ μm], the peak of mode 1 broadens due to the pinning vortical flow at this confinement. As the system transitions towards bulk turbulence [panel c; $W = 76$ μm], the flow energy shifts to the walls—demonstrating the previously reported coherent, near-wall activity [18]—and the higher-order modes now contribute significantly to the central portion of the channel.

The energy spectrum $E(k)$ in 2D [Fig. 2(a)] was calculated through the Wiener-Khinchine theorem [4] as the Fourier transformation of the equal-time two-point velocity correlation function:

$$E(k) = \frac{k}{2\pi}\int d^2\mathrm{Re}^{-i\mathbf{k}\cdot\mathbf{R}}\langle\mathbf{v}(\mathbf{r}, t) \cdot \mathbf{v}(\mathbf{r} + \mathbf{R}, \mathbf{t})\rangle.$$

Autocorrelation functions (ACFs) for a given field $\chi(\mathbf{r}, t)$ were calculated as the mean time-averaged two-point correlation:

$$C_r(\Delta r) = \frac{\langle\chi(\mathbf{r}, t) \cdot \chi(\mathbf{r} + \Delta r, t)\rangle}{\langle\chi^2(\mathbf{r}, t)\rangle},$$

where χ is $\mathbf{v}$ or ϕ, and the correlation length δ is defined as $C_r(\Delta r = \delta) = 1/e$.

4. Cell suspensions under varying confinement

To quantify POD modes for bacterial suspensions under varying degrees of confinement (Fig. 3), experiments from Ref. [18] were replicated with minor modifications. Microfluidic devices (19 μm deep) were fabricated, which comprised a series of racetrack geometries connected by narrow inlets (30 μm wide). Nine racetrack widths were chosen between 30 μm $\leqslant W \leqslant$ 171 μm in fractional increments of our measured characteristic vortex size (38 μm) taken as the minimum point in the spatial ACF under quasi-2D conditions [Fig. 1(d), dotted red line). Cell suspensions were imaged

at 40× (0.6 NA) magnification and 100 fps for 10 s per channel width. All confined microfluidic geometries were simultaneously loaded with the same cell suspension and imaged within the first 10 min of loading to ensure consistent bacterial activity. Experiments were repeated across multiple days with freshly cultured bacteria to verify repeatability. The net flow ψ was calculated following the definition in Ref. [18]: $\psi = |(\Sigma \mathbf{u} \cdot \hat{\mathbf{e}}_x)/(\Sigma||\mathbf{u}||)|$, where $\hat{\mathbf{e}}_x$ is the unit vector along the principal channel direction and the sum is over all PIV subwindows over 5 s (500 frames) of video. $\psi = 1$ indicates unidirectional circulation flow around the racetrack, and $\psi = 0$ corresponds to a globally stationary suspension. The streamwise flow profiles, $F(y)$, were generated from the velocity field by averaging over time and space as $F(y) = \langle \mathbf{u}(x, y, t) \cdot \hat{\mathbf{e}}_x \rangle_{(x,t)}$, where $\hat{\mathbf{e}}_x$ was chosen as defined in Ref. [18], such that $F(y)$ is on average positive.

5. Cell suspensions under externally imposed flow

The data corresponding to Fig. 4 were obtained from a previously published work [43]; the relevant experimental details are repeated here for convenience. Dense suspensions ($\approx$1.3–2 $\times$ 10^{10} cells/ml) of wild-type *B. subtilis* (strain OI1085) were flowed through a PDMS microfluidic chamber (200 μm wide × 320 μm deep) via a syringe pump at a flow rate of $Q = 25$ μl/h. Imaging was performed under brightfield conditions at 30× magnification. For motile cell suspensions, 19 individual videos (4-s duration) were acquired at 370 fps. Velocity fields were quantified through ghost particle velocimetry [70] and averaged such that each pixel is the average of 32 × 32 pixel square over 50 frames. Image data and velocity fields for nonmotile cell suspensions were acquired under the same conditions, but with a dead suspension of *B. subtilis*. Vortical regions in the flow were identified using the Okubo-Weiss parameter [71,72] for manual tracking of traveling flow structures.

APPENDIX B: SUPPORTING FIGURES

This Appendix contains the supporting figures (Figs. 5–7).

[1] M. Nagy, Z. Ákos, D. Biro, and T. Vicsek, Hierarchial group dynamics in pigeon flocks, Nature (London) **464**, 890 (2010).
[2] B. L. Partridge, J. Johansson, and J. Kalish, The structure of schools of giant bluefin tuna in Cape Cod Bay, Environ. Biol. Fishes **9**, 253 (1983).
[3] C. Dombrowski, L. Cisneros, S. Chatkaew, R. E. Goldstein, and J. O. Kessler, Self-Concentration and Large-Scale Coherence in Bacterial Dynamics, Phys. Rev. Lett. **93**, 098103 (2004).
[4] H. H. Wensink, J. Dunkel, S. Heidenreich, K. Drescher, R. E. Goldstein, H. Löwen, and J. M. Yeomans, Meso-scale turbulence in living fluids, Proc. Natl. Acad. Sci. USA **109**, 14308 (2012).
[5] P. Liu, Z. Hongwei, Z. Ying, D. Guangle, N. Luhui, W. Dunyou, C. Ke, L. Ying, Z. Ning, Y. Fangfu, and Y. Mingcheng, Oscillating collective motion of active rotors in confinement, Proc. Natl. Acad. Sci. USA **117**, 11901 (2020).
[6] J. Bures, J. Cyrany, D. Kohoutova, M. Förstl, S. Rejchrt, J. Kvetina, V. Vorisek, and M. Kopacova, Small intestinal bacterial overgrowth syndrome, World J. Gastroenterol. **16**, 2978 (2010).
[7] J. Brugués and D. Needleman, Physical basis of spindle self-organization, Proc. Natl. Acad. Sci. USA **111**, 18496 (2014).
[8] J. Gachelin, A. Rousselet, A. Lindner, and E. Clement, Collective motion in an active suspension of *Escherichia coli* bacteria, New J. Phys. **16**, 025003 (2014).
[9] R. Colin, K. Drescher, and V. Sourjik, Chemotactic behaviour of *Escherichia coli* at high cell density, Nat. Commun. **10**, 5329 (2019).
[10] A. Sokolov, I. S. Aranson, J. O. Kessler, and R. E. Goldstein, Concentration Dependence of the Collective Dynamics of Swimming Bacteria, Phys. Rev. Lett. **98**, 158102 (2007).

[11] A. Sokolov and I. S. Aranson, Physical Properties of Collective Motion in Suspensions of Bacteria, Phys. Rev. Lett. **109**, 248109 (2012).
[12] J. Dunkel, S. Heidenreich, K. Drescher, H. H. Wensink, M. Bär, and R. E. Goldstein, Fluid Dynamics of Bacterial Turbulence, Phys. Rev. Lett. **110**, 228102 (2013).
[13] X.-L. Wu and A. Libchaber, Particle Diffusion in a Quasi-Two-Dimensional Bacterial Bath, Phys. Rev. Lett. **84**, 3017 (2000).
[14] R. Alert, J. Casademunt, and J.-F. Joanny, Active turbulence, Annu. Rev. Condens. Matter Phys. **13**, 143 (2022).
[15] G. K. Batchelor and C. U. Press, *The Theory of Homogeneous Turbulence*, Cambridge Science Classics (Cambridge University, Cambridge, England, 1953).
[16] M. J. Kim and K. S. Breuer, Enhanced diffusion due to motile bacteria, Phys. Fluids **16**, L78 (2004).
[17] H. Wioland, F. G. Woodhouse, J. Dunkel, J. O. Kessler, and R. E. Goldstein, Confinement Stabilizes a Bacterial Suspension into a Spiral Vortex, Phys. Rev. Lett. **110**, 268102 (2013).
[18] H. Wioland, E. Lushi, and R. E. Goldstein, Directed collective motion of bacteria under channel confinement, New J. Phys. **18**, 075002 (2016).
[19] A. Sokolov and I. S. Aranson, Reduction of Viscosity in Suspension of Swimming Bacteria, Phys. Rev. Lett. **103**, 148101 (2009).
[20] H. M. López, J. Gachelin, C. Douarche, H. Auradou, and E. Clément, Turning Bacteria Suspensions into Superfluids, Phys. Rev. Lett. **115**, 028301 (2015).
[21] A. E. Hamby, D. K. Vig, S. Safonova, and C. W. Wolgemuth, Swimming bacteria power microspin cycles, Sci. Adv. **4**, eaau0125 (2018).
[22] W. Chen, N. Mani, H. Karani, H. Li, S. Mani, and J. X. Tang, Confinement discerns swarmers from planktonic bacteria, eLife **10**, e64176 (2021).
[23] H. Du, W. Xu, Z. Zhang, and X. Han, Bacterial behavior in confined spaces, Front. Cell Dev. Biol. **9**, 629820 (2021).
[24] Y. Peng, Z. Liu, and X. Cheng, Imaging the emergence of bacterial turbulence: Phase diagram and transition kinetics, Sci. Adv. **7**, eabd1240 (2021).
[25] D. L. Koch and G. Subramanian, Collective hydrodynamics of swimming microorganisms: Living fluids, Annu. Rev. Fluid Mech. **43**, 637 (2011).
[26] C. W. Wolgemuth, Collective swimming and the dynamics of bacterial turbulence, Biophys. J. **95**, 1564 (2008).
[27] A. Baskaran and M. C. Marchetti, Hydrodynamics of self-propelled hard rods, Phys. Rev. E **77**, 011920 (2008).
[28] D. Saintillan and M. J. Shelley, Instabilities and Pattern Formation in Active Particle Suspensions: Kinetic Theory and Continuum Simulations, Phys. Rev. Lett. **100**, 178103 (2008).
[29] A. Doostmohammadi, T. N. Shendruk, K. Thijssen, and J. M. Yeomans, Onset of meso-scale turbulence in active nematics, Nat. Commun. **8**, 15326 (2017).
[30] R. Supekar, B. Song, A. Hastewell, G. P. T. Choi, A. Mietke, and J. Dunkel, Learning hydrodynamic equations for active matter from particle simulations and experiments, Proc. Natl. Acad. Sci. USA **120**, e2206994120 (2023).
[31] P. A. H. Westley, A. M. Berdahl, C. J. Torney, and D. Biro, Collective movement in ecology: from emerging technologies to conservation and management, Philos. Trans. R. Soc., B **373**, 20170004 (2018).
[32] E. S. Bililign, F. Balboa Usabiaga, Y. A. Ganan, A. Poncet, V. Soni, S. Magkiriadou, M. J. Shelley, D. Bartolo, and W. T. M. Irvine, Motile dislocations knead odd crystals into whorls, Nat. Phys. **18**, 212 (2022).
[33] J. L. Lumley, The structure of inhomogeneous turbulent flows, in *Atmospheric Turbulence and Radio Wave Propagation*, edited by A. M. Yaglom and V. I. Tartarsky (Nauka, Moscow, 1967), pp. 166–177.
[34] G. Berkooz, P. Holmes, and J. L. Lumley, The proper orthogonal decomposition in the analysis of turbulent flows, Annu. Rev. Fluid Mech. **25**, 539 (1993).
[35] Y. C. Liang, H. P. Lee, S. P. Lim, W. Z. Lin, K. H. Lee, and C. G. Wu, Proper orthogonal decomposition and its applications—Part I: Theory, J. Sound Vib. **252**, 527 (2002).

[36] L. Sirovich and M. Kirby, Low-dimensional procedure for the characterization of human faces, J. Opt. Soc. Am. A **4**, 519 (1987).
[37] K. Taira, S. L. Brunton, S. T. Dawson, C. W. Rowley, T. Colonius, B. J. McKeon, O. T. Schmidt, S. Gordeyev, V. Theofilis, and L. S. Ukeiley, Modal analysis of fluid flows: An overview, AIAA J. **55**, 4013 (2017).
[38] A. Chatterjee, An introduction to the proper orthogonal decomposition, Curr. Sci. **78**, 808 (2000).
[39] H. Ding, C. Shu, K. S. Yeo, and D. Xu, Numerical simulation of flows around two circular cylinders by mesh-free least square-based finite difference methods, Int. J. Numer. Methods Fluids **53**, 305 (2007).
[40] J. E. Higham, M. Shahnam, and A. Vaidheeswaran, Using a proper orthogonal decomposition to elucidate features in granular flows, Granular Matter **22**, 86 (2020).
[41] Â. M. Ribau, N. D. Gonçalves, L. L. Ferrás, and A. M. Afonso, Flow structures identification through proper orthogonal decomposition: The flow around two distinct cylinders, Fluids **6**, 384 (2021).
[42] P. Gutierrez-Castillo and B. Thomases, Proper orthogonal decomposition (POD) of the flow dynamics for a viscoelastic fluid in a four-roll mill geometry at the Stokes limit, J. Non-Newtonian Fluid Mech. **264**, 48 (2019).
[43] E. Secchi, R. Rusconi, S. Buzzaccaro, M. M. Salek, S. Smriga, R. Piazza, and R. Stocker, Intermittent turbulence in flowing bacterial suspensions, J. R. Soc. Interface **13**, 20160175 (2016).
[44] L. Sirovich, Chaotic dynamics of coherent structures, Phys. D (Amsterdam, Neth.) **37**, 126 (1989).
[45] Y. Wang, L. Wang, R. Hu, L. Kong, and J. Cheng, Effects of sampling frequency on the proper orthogonal decomposition based reconstruction of a wind turbine wake, IET Renewable Power Gen. **15**, 2956 (2021).
[46] P. Premaratne, W. Tian, and H. Hu, A proper-orthogonal-decomposition (POD) study of the wake characteristics behind a wind turbine model, Energies **15**, 3596 (2022).
[47] J. B. Freund and T. Colonius, Turbulence and sound-field POD analysis of a turbulent jet, Int. J Aeroacoustics **8**, 337 (2009).
[48] D. Butcher and A. Spencer, Cross-correlation of POD spatial modes for the separation of stochastic turbulence and coherent structures, Fluids **4**, 134 (2019).
[49] Y. Wang, W.-H. Cai, T.-Z. Wei, H.-N. Zhang, L. Wang, and F.-C. Li, Proper orthogonal decomposition analysis for two-oscillating grid turbulence with viscoelastic fluids, Adv. Mech. Eng. **8**, 11 (2016).
[50] A. Doostmohammadi, J. Ignés-Mullol, J. M. Yeomans, and F. Sagués, Active nematics, Nat. Commun. **9**, 3246 (2018).
[51] H. Wioland, F. G. Woodhouse, J. Dunkel, and R. E. Goldstein, Ferromagnetic and antiferromagnetic order in bacterial vortex lattices, Nat. Phys. **12**, 341 (2016).
[52] A. Opathalage, M. M. Norton, M. P. N. Juniper, B. Langeslay, S. A. Aghvami, S. Fraden, and Z. Dogic, Self-organized dynamics and the transition to turbulence of confined active nematics, Proc. Natl. Acad. Sci. USA **116**, 4788 (2019).
[53] S. Čoplar, J. Aplinc, Ž. Kos, S. Žumer, and M. Ravnik, Topology of Three-Dimensional Active Nematic Turbulence Confined to Droplets, Phys. Rev. X **9**, 031051 (2019).
[54] Z. You, D. J. G. Pearce, and L. Giomi, Confinement-induced self-organization in growing bacterial colonies, Sci. Adv. **7**, eabc8685 (2021).
[55] S. Coppola and V. Kantsler, Curved ratchets improve bacteria rectification in microfluidic devices, Phys. Rev. E **104**, 014602 (2021).
[56] M. Theillard, R. Alonso-Matilla, and D. Saintillan, Geometric control of active collective motion, Soft Matter **13**, 363 (2017).
[57] P. J. Schmid, Dynamic mode decomposition of numerical and experimental data, J. Fluid Mech. **656**, 5 (2010).
[58] A. Loisy, J. Eggers, and T. B. Liverpool, Active Suspensions Have Nonmonotonic Flow Curves and Multiple Mechanical Equilibria, Phys. Rev. Lett. **121**, 018001 (2018).
[59] W. Wang and R. Zhang, Interplay of active stress and driven flow in self-assembled, tumbling active nematics, Crystals **11**, 1071 (2021).
[60] R. Vitkovicova, Y. Yokoi, and T. Hyhlik, Identification of structures and mechanisms in a flow field by POD analysis for input data obtained from visualization and PIV, Exp. Fluids **61**, 171 (2020).
[61] A. K. M. F. Hussain, Coherent structures and turbulence, J. Fluid Mech. **173**, 303 (1986).

[62] W. Brevis and M. García-Villalba, Shallow-flow visualization analysis by proper orthogonal decomposition, J. Hydraul. Res. **49**, 586 (2011).
[63] P. J. Schmid, L. Li, M. P. Juniper, and O. Pust, Applications of the dynamic mode decomposition, Theor. Comput. Fluid Dyn. **25**, 249 (2011).
[64] C.-Y. Ohh and G. R. Spedding, Wake identification of stratified flows using dynamic mode decomposition, Phys. Rev. Fluids **7**, 024801 (2022).
[65] D. W. Ashmore, D. W. F. Mair, J. E. Higham, S. Brough, J. M. Lea, and I. J. Nias, Proper orthogonal decomposition of ice velocity identifies drivers of flow variability at Sermeq Kujalleq (Jakobshavn Isbræ), The Cryosphere **16**, 219 (2022).
[66] H. Li, X. qing Shi, M. Huang, X. Chen, M. Xiao, C. Liu, H. Chaté, and H. P. Zhang, Data-driven quantitative modeling of bacterial active nematics, Proc. Natl. Acad. Sci. USA **116**, 777 (2019).
[67] D. Floryan and M. D. Graham, Discovering multiscale and self-similar structure with data-driven wavelets, Proc. Natl. Acad. Sci. USA **118**, e2021299118 (2021).
[68] Y. Xia and G. M. Whitesides, Soft lithography, Annu. Rev. Mater. Sci. **28**, 153 (1998).
[69] W. Thielicke and E. J. Stamhuis, PIVlab—Towards user-friendly, affordable and accurate digital particle image velocimetry in MATLAB, J. Open Res. Software **2**, e30 (2014).
[70] S. Buzzaccaro, E. Secchi, and R. Piazza, Ghost Particle Velocimetry: Accurate 3D Flow Visualization Using Standard Lab Equipment, Phys. Rev. Lett. **111**, 048101 (2013).
[71] A. Okubo, Horizontal dispersion of floatable particles in the vicinity of velocity singularities such as convergences, Deep-Sea Res. Oceanogr. Abstr. **17**, 445 (1970).
[72] P. Perlekar, S. S. Ray, D. Mitra, and R. Pandit, Persistence Problem in Two-Dimensional Fluid Turbulence, Phys. Rev. Lett. **106**, 054501 (2011).